

# Realizing Double Graded CIGSe Absorbers With the R2R Hybrid-CIGSe-Process

Nikolaus Weinberger , David Stock, Jochen Mesle, Christian A. Kaufmann , Tobias Bertram, Tim Kodalle , Roland Wuerz, Daniel Huber, Andreas Zimmermann, Georg Strauss, and Roman Lackner

**Abstract**—This article presents an approach for industrial roll-to-roll (R2R) deposition of Cu(In,Ga)Se<sub>2</sub> (CIGSe) thin films on stainless steel foil for use as absorber layers in flexible thin-film solar cells. The hybrid-CIGSe-deposition-process combines magnetron sputtering with evaporation techniques and allows the realization of a double graded CIGSe layer, reaching a conversion efficiency of currently up to 14.0% (w/o antireflective coating). The influence of different power settings of the individual magnetrons on the gallium profile is described. For a deeper understanding of differences between a static and an R2R process, a calculated flux diagram is presented. In the second part of this contribution, the homogeneity of the industrial scale samples is discussed by comparing the change in *CGI* and *GGI* over the foil width of 30 cm. The hybrid-CIGSe-deposition-process excels in a straightforward scalability for industrial usage due to the application of planar magnetron sputtering sources as metal vapor supply.

**Index Terms**—*CGI*, CIGSe, Cu<sub>2</sub>Se, evaporation, flexible PV, glow-discharge optical emission spectrometry (GD-OES), *GGI*, GI-XRD, industrial approach, magnetron sputtering, roll-to-roll (R2R) processing, SEM.

## I. INTRODUCTION

CIGSe thin-film devices have not only reached a competitive record efficiency of 23.35% as a single junction cell [1], but have also demonstrated suitability as bottom cells in highly efficient multijunction solar cells [2], [3]. These achievements

Manuscript received October 16, 2020; revised December 2, 2020; accepted December 9, 2020. Date of publication January 8, 2021; date of current version February 19, 2021. This work was supported in part by Austrian Research Promotion Agency (FFG) and in part by the Klima und Energiefonds under Grant KR18EF0F14235. (Corresponding author: Nikolaus Weinberger.)

Nikolaus Weinberger, David Stock, Jochen Mesle, and Georg Strauss are with the Material Center Tyrol, Department of Structural Engineering and Material Sciences, University of Innsbruck, 6020 Innsbruck, Austria (e-mail: nikolaus.weinberger@uibk.ac.at; david.stock@uibk.ac.at; jochen.mesle@uibk.ac.at; georg.strauss@uibk.ac.at).

Christian A. Kaufmann, Tobias Bertram, and Tim Kodalle are with the Competence Centre Photovoltaics Berlin, Helmholtz-Zentrum Berlin für Materialien und Energie, 14109 Berlin, Germany (e-mail: kaufmann@helmholtz-berlin.de; tobias.bertram@helmholtz-berlin.de; tim.kodalle@helmholtz-berlin.de).

Roland Wuerz is with Zentrum für Sonnenenergie- und Wasserstoff-Forschung Baden-Württemberg, 70563 Stuttgart, Germany (e-mail: roland.wuerz@zsw-bw.de).

Daniel Huber and Andreas Zimmermann are with the Sunplugged GmbH, 6030 Schwaz, Austria (e-mail: daniel.huber@sunplugged.at; andreas.zimmermann@sunplugged.at).

Roman Lackner is with Unit of Material Technology, Department of Structural Engineering and Material Sciences, University of Innsbruck, 6020 Innsbruck, Austria (e-mail: roman.lackner@uibk.ac.at).

Color versions of one or more of the figures in this article are available online at <https://doi.org/10.1109/JPHOTOV.2020.3045674>.

Digital Object Identifier 10.1109/JPHOTOV.2020.3045674

may lead to a larger demand of CIGSe material for commercial solar devices in the near future. Therefore, the development of efficient and stable processes for industrial application gains importance. A promising approach is the hybrid-CIGSe-deposition-process, developed by the company Sunplugged GmbH, the Material Center Tyrol (MCT), the company DePro Control GmbH, and the University Milano-Bicocca. The R2R deposition technique combines magnetron sputtering with evaporation techniques and its major advantage is a straightforward scalability. Homogeneity over the entire foil width is realized by using planar pure metal targets. The basic concept for the hybrid-process was developed by Acciarri *et al.* [4]–[6] for laboratory scale static deposition. Previous deposition of CIGSe absorber layers with the R2R hybrid-CIGSe-process [7] resulted in a conversion efficiency of > 10%.

This contribution focuses on the introduction of gallium in the process to form alloyed CIGSe layers with the R2R hybrid-CIGSe-process. It is based on the proceeding [8] of the 47th IEEE-PVSC. The extension to the proceeding focuses on the evaluation of the resulting homogeneity in view of industrial application and gives detailed insight in the basics of the R2R hybrid-CIGSe-process.

## II. EXPERIMENTAL

### A. Solar Cell Fabrication

A 30-cm-wide stainless-steel foil with a sol-gel based dielectric insulation layer with a composition of 94 at% SiO<sub>2</sub> and 6 at% K<sub>2</sub>O is used as substrate; further details are in [9]. The back-contact consists of a tri-layer of titanium, sodium doped as well as pristine molybdenum. The layer stack is deposited by magnetron sputtering in a self-built R2R deposition machine. Subsequently, the absorber is grown onto the back contact stack in a separate R2R deposition chamber.

Absorbers for Sunplugged's devices are produced with the hybrid-CIGSe-process. Thereby, the deposition chamber is divided into three zones to realize the concept of a three-stage codeposition process in R2R configuration. The first and third zones are each equipped with both a gallium and an indium target and the second zone with two copper targets. Every zone consists of a sector for magnetron sputtering, a cylindrical transfer device (CTD), and an evaporation region. Each CTD consists of 60 graphite bars, arranged in a cylindrical geometry. A photograph of a lab-scale version of the CTD is shown in [6]. Initially, the metals are deposited onto the CTD by magnetron

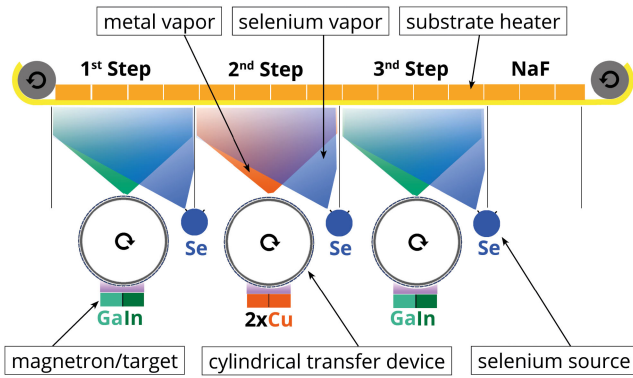


Fig. 1. Schematic top view of Sunplugged's CI(G)Se deposition process. Metal components are sputtered on graphite bars and subsequently evaporated and deposited on a steel substrate. Selenium is introduced by temperature-controlled effusion cells.

sputtering. This requires an argon pressure of  $\sim 3 \times 10^{-3}$  mbar to be present in the deposition chamber. After the metal deposition, the graphite bars rotate to point in the direction of the substrate. There, the metal is thermally evaporated from the bars and deposited onto the substrate in selenium atmosphere. Through stepwise rotation and subsequent individual application of current to the graphite bars, the evaporating metals create a periodical flux profile. The power applied to the respective magnetron controls the amplitude of the particle flux of the individual metals. Selenium is introduced to the evaporation zone of the chamber by three temperature-controlled effusion cells. In the first zone, the temperature of the substrate is set to nominally 400 °C, while in Zones 2 and 3 the temperature was increased to nominally 550 °C. A scheme of the deposition setup is shown in Fig. 1, with further details described in [7]. Fig. 2 should help to understand the challenge to adjust the particle flux distributions of the individual elements in an R2R process. In contrast to a non-R2R process, it is not possible to use only the “sweet spot” of the flux distributions. Therefore, the adjustment of the individual flux distributions, especially to form a suitable gallium gradient, is of high importance.

After absorber deposition, the devices are completed by the application of a chemical bath deposited CdS buffer layer, an intermediate i-ZnO layer, and a tin-doped indium oxide (ITO) front contact, both deposited by magnetron sputtering. To facilitate current collection, Al/Ni/Al contact fingers were deposited via e-beam evaporation. Finally, the layers were mechanically separated into cells of about 1 cm<sup>2</sup> in size. The addition of contact fingers and the cell separation were performed at Helmholtz-Zentrum Berlin (HZB), whereas all other layers were deposited at Sunplugged.

For each sample, 60 individual solar cells are fabricated along the central  $\sim 20$ -cm-wide region of the 30-cm-wide substrate foil (see also Fig. 7).

### B. Analytical Methods

In order to characterize the compositional in-depth gradients in the CI(G)Se absorber, glow-discharge optical emission

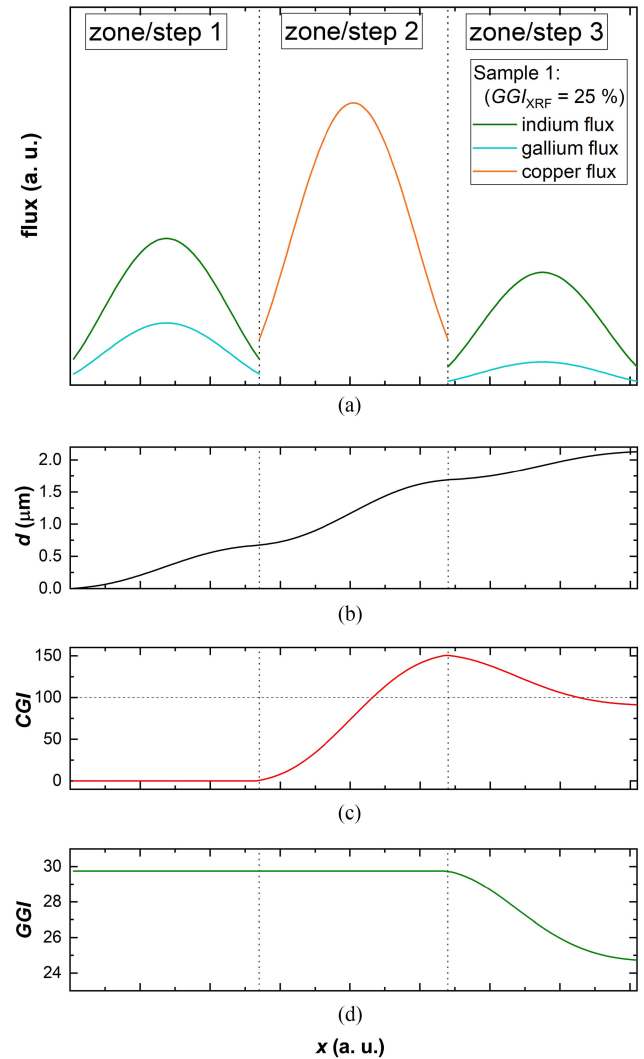


Fig. 2. (a) Flux-diagram of Sample 1 ( $GGI_{XRF} = 25\%$ ) of the R2R hybrid-CIGSe-process. The bottom  $x$ -axis shows the position of the sample in the CI(G)Se deposition machine. (b) Resulting layer thickness. (c) Evolution of the total  $CGI$ . (d) Evolution of the total  $GGI$ ; The distance  $x$  can be substituted by the time  $t$  using the relation  $t = x/v_{sub}$ , with  $v_{sub}$  being the velocity of the substrate.

spectrometry (GD-OES) measurements were performed at HZB and ZSW. The quantification was done following the procedure described in [10]. Current–voltage ( $jV$ )-measurements were performed under AM1.5 illumination at 25 °C using a Wacom class AAA sun simulator at standard conditions. Wavelength dispersive X-ray fluorescence spectrometry (WDXRF) was performed using a Rigaku Primus III+, to determine elemental composition and layer thickness. For the measurements in Table I, a circular aperture of 30 mm was used, while for the analysis of the homogeneity in Fig. 6, a 10 mm aperture was applied. Intensities of the K-shells were considered for all analyzed elements, using an excitation energy of 50 keV. The quantification was done by the fundamental parameter method developed by Rigaku. X-ray diffraction (GI-XRD) measurements were performed at a Panalytical Empyrean with parallel beam optics. 30 keV and 50 mA were used as source settings, the incident beam angle  $\Omega$

TABLE I  
SAMPLE SUMMARY; VALUES EVALUATED BY WDXRF;  $d_{\text{XRF}}$  IS THE THICKNESS OF THE ABSORBER

sample selection – WDXRF values			
#	$GGI_{\text{XRF}}$ (%)	$d_{\text{XRF}}$ ( $\mu\text{m}$ )	$CGI_{\text{XRF}}$ (%)
1	25	2.127	91
2	31	2.076	96
3	43	1.926	84
4	48	1.884	89

was set to  $1^\circ$  for the comparative measurements in Fig. 10 and was varied between  $0.2^\circ$  and  $3^\circ$  for the in-depth measurements in Fig. 11. A Jeol 7610F scanning electron microscope (SEM) equipped with an EDX and a backscatter detector came into operation for surface morphology evaluation. External quantum efficiency (EQE) measurements were performed on a custom built instrument at HZB.

### III. RESULTS AND DISCUSSION

#### A. Formation and Evaluation of Gallium Profile

A particle flux diagram has been calculated of the hybrid-CIGSe-process as described in [7] and is shown in Fig. 2. The main difference to a static process becomes apparent when the shape of the flux distributions is taken into account. These are mainly determined by the geometrical layout of the deposition chamber. In addition to the flux distributions, the time-dependent layer thickness, the cumulative, and elemental copper-to-indium plus gallium ( $CGI = [\text{Cu}]/([\text{Ga}]+[\text{In}])$ ) and the gallium-to-gallium plus indium ratios ( $GGI = [\text{Ga}]/([\text{Ga}]+[\text{In}])$ ) were calculated. This was exemplarily done for a set of deposition parameters of Sample 1 (see Table I). It must be mentioned that re-evaporation from surfaces, including the substrate, are neglected in the simulation. Further details on the calculations can be found in [7].

In this work, four CIGSe absorber layers with different gallium content are compared. The integral compositions as measured by WDXRF are summarized in Table I. The  $GGI$  in-depth profiles by GD-OES resulting from the different deposition conditions are shown in Fig. 3. The  $GGI_{\text{step1}}$  at the bottom of the absorber layer, close to the CIGSe/Mo interface, correlates with the ratio of the power of the Ga and In magnetron in the first step ( $PR_{\text{step1}}$ ). The  $GGI_{\text{step3}}$  at the top of the absorber layer is mainly influenced by the power ratio in the third step ( $PR_{\text{step3}}$ ). The  $PR$  value is defined according to following equation:

$$PR_{\text{step } i=1,3} = \frac{P_i^{\text{Ga}}}{(P_i^{\text{Ga}} + P_i^{\text{In}})} \quad (1)$$

where  $P$  is the power applied to the particular magnetron/target, and the subscripts name the type of metal and the geometric position. The resulting linear dependency between  $PR$  and  $GGI$  is shown in Fig. 4; it has to be mentioned that eight additional  $GGI$  profiles to the plotted profiles in Fig. 3 have been considered. Consequently, a decent control of the  $GGI$  profile by the  $PR$  using the hybrid-CIGSe-process can be assumed.

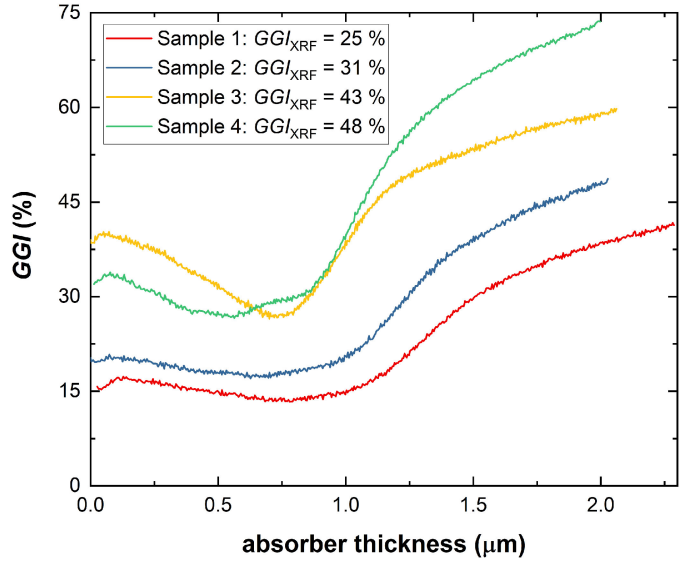


Fig. 3. Depth profile of the  $GGI$  of four different CIGSe layers, as measured by GD-OES.

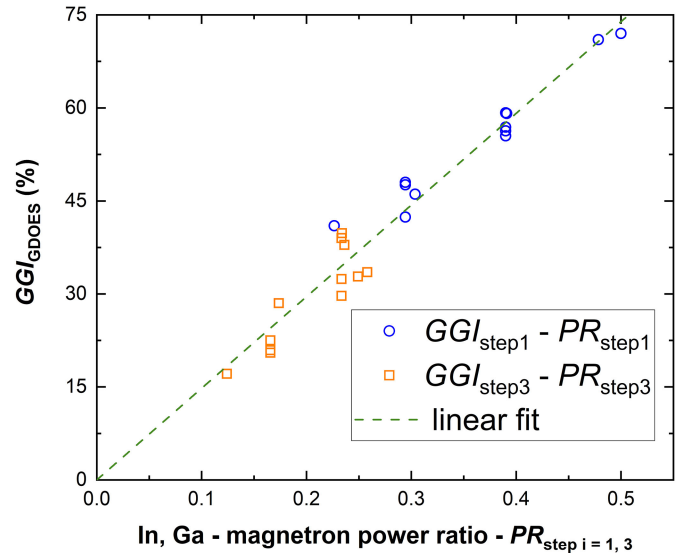


Fig. 4.  $GGI_{\text{step1/3}}$ , extracted from GD-OES measurements (in total 12  $GGI$  profiles) are plotted against the power ratio of the magnetrons  $PR_{\text{step } i=1,3}$ . A linear dependency is found, which implies good control of the Ga profile in the R2R Hybrid-CIGSe-process.

The highest active area, lab-scale cell efficiency achieved with the R2R hybrid-CIGSe-process at Sunplugged GmbH up until now is 14.0% (w/o antireflective coating, active area). The  $j$ - $V$ -curves and EQE measurement of the best cells of the four samples with different Ga depth profiles are shown in Fig. 5. The device data of the best cells of each sample are summarized in Table II. The efficiency was calculated using  $j_{\text{EQE}}$ , i.e., the active area efficiencies are given. For the box plots in Fig. 6, however, the  $j_{\text{SC}}$  values were used. While  $V_{\text{OC}}$  increases,  $j_{\text{SC}}$  decreases with higher  $GGI$ . It has to be pointed out that Sample 3 has a lower  $j_{\text{SC}}$  than Sample 4, even though its integral gallium content is lower. This may be caused by the sharper and narrower

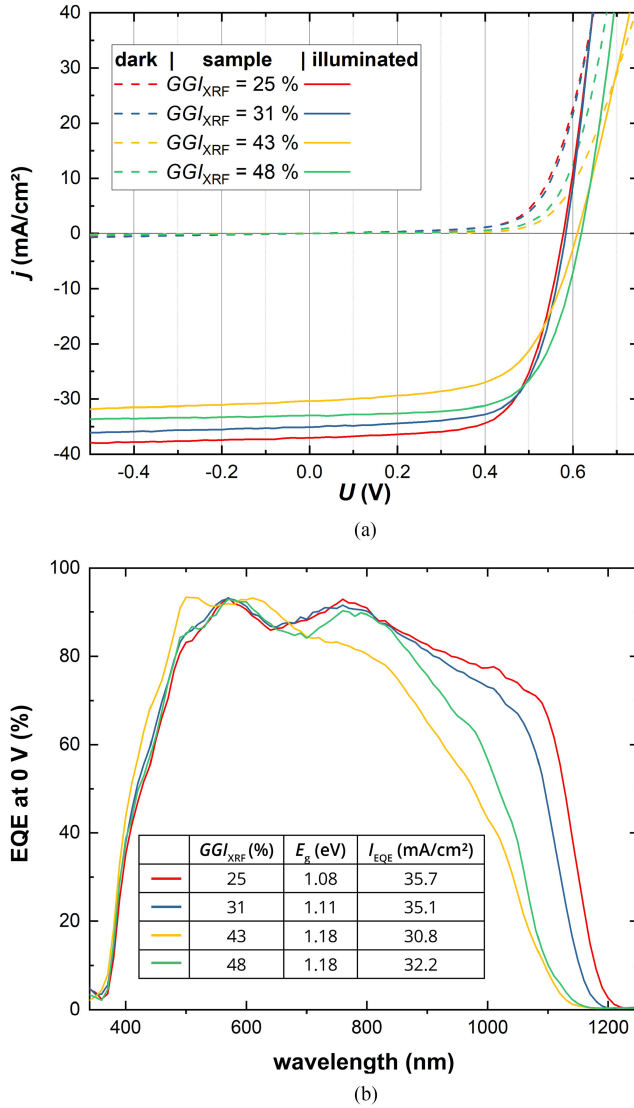


Fig. 5. (a)  $jV$ -curves (dark and illuminated) of the best cells of the four samples. (b) EQE of the four samples, showing a correlation to the minimum  $GGI$  of the GD-OES profiles (see Fig. 3).

notch-region, the flatter  $GGI$  in the region near the back contact, and due to the lowest integral  $CGI$ , which results in a thicker copper poor vacancy compound (VC) at the CIGSe surface. Due to its lower bandgap, a thicker VC would also explain a lower current collection for higher wavelengths [11], [12], which can be seen in the EQE measurements. Additionally, the difference between the lowest  $GGI$  at about 700 nm depth (from surface) and the  $GGI$  at the surface is higher when compared to the other three samples, which might lead to an electrical barrier for the photo-generated electrons. The latter might also be the reason for the slightly reduced fill factor ( $FF$ ) of Sample 3. Considering that the evaluated  $j_{EQE}$  for Sample 3 is slightly lower than  $j_{SC}$ , it should be mentioned that due to the mechanical scribing step, the cell area generally carries an error of  $\pm 10\%$ . The EQE of Sample 3 shows different reflection interference, even though the top layers were performed in the same batch. This again

TABLE II  
 $J_{SC}$ ,  $V_{OC}$ ,  $FF$ ,  $\eta$  (ACTIVE AREA) CALCULATED WITH  $J_{EQE}$ ,  $J_{EQE}$ , AND  $E_g$  OF THE BEST CELLS OF THE FOUR SAMPLES

summary of device data							
#	$GGI$ (%)	$j_{SC}$ ( $\text{mA}/\text{cm}^2$ )	$V_{oc}$ (mV)	$FF$ (%)	$\eta$ (%)	$j_{EQE}$ ( $\text{mA}/\text{cm}^2$ )	$E_g$ (eV)
1	25	37.0	578	67	13.8	35.7	1.08
2	31	35.1	584	68	14.0	35.1	1.11
3	43	30.7	609	61	11.3	30.8	1.18
4	48	33.0	619	66	13.2	32.2	1.18

Notes: One can see the influence of the  $GGI$  on the increase of the  $V_{OC}$  and a decrease of the  $j_{SC}$ . The differences between  $j_{SC}$  and  $j_{EQE}$  arise from difficulties of the mechanical structuring of the cells.

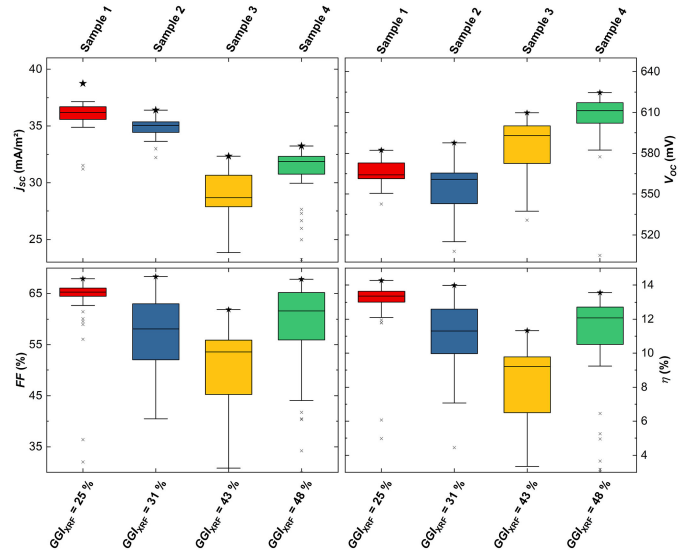


Fig. 6. Box plots of the  $jV$  data. With increasing  $GGI$ ,  $j_{SC}$  is decreased,  $V_{OC}$  increases. For Sample 2, the bottom region where the  $CGI$  is higher than 100% (described in the next section) is not included in the statistics.

might be caused by a comparatively thicker VC at the absorber's surface [11], [12]. In general, the evaluated bandgap of EQE measurements shows a direct dependency to the minimum of the  $GGI$  extractable from Fig. 3. In our opinion, the most promising  $GGI$  gradient is either of Sample 1 or Sample 2. Especially, if the CIGSe layer is applied as a bottom cell for tandem devices in the near future, where lower bandgap CIGSe absorbers are considered to be more suitable.

### B. Challenge of Homogeneity

We would like to give a more detailed insight in the performance of Sample 1 and Sample 2, using position-dependent data to highlight aspects concerning the homogeneity of the analyzed samples. The following section discusses WDXRF measurements across the entire foil width, 3 cm apart of each other and measured with a circular aperture of 1 cm diameter. Additionally, GD-OES profiles, SEM pictures, and GI-XRD measurements were conducted in the top, middle (mid), and bottom (bot) regions. These data are compared to the position dependent device measurements shown in Fig. 7.

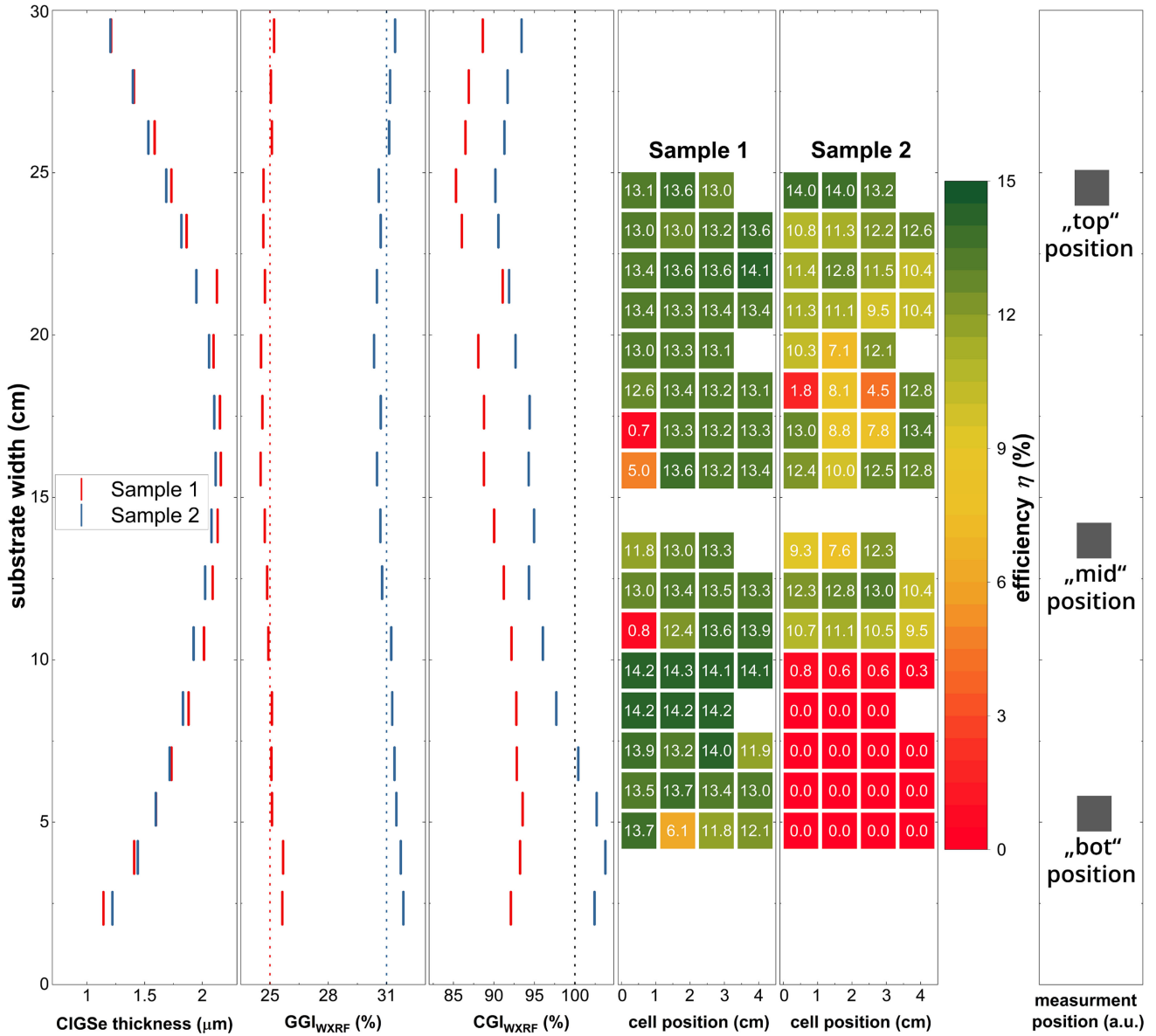


Fig. 7. CIGSe thickness,  $GGI$ , and  $CGI$  of Samples 1 and 2 as determined by WDXRF as a function of the position over the bandwidth. Furthermore, the device efficiency as a function of position is shown for Samples 1 and 2. We analyzed about 21 cm of the 30-cm-wide substrate. While Sample 1 shows a good homogeneity, Sample 2 exhibits a strong decrease in efficiency from top to bottom down to 0% at the bottom region. The cells have approximately an area of 1  $\text{cm}^2$  each. In the white areas, no cells were fabricated. The extreme right plot indicates the position of further measurements (GI-XRD and GD-OES).

In contrast to the  $CGI$ , we can clearly identify a constant  $GGI$  over the analyzed foil width, measured by WDXRF, with a deviation of less than 1%. For the  $CGI$ , it shows a difference of up to 30% across the foil width for both samples, Samples 1 and 2. The higher  $CGI$  is located at the bottom of the samples. We also clearly see that the thickness of the absorber varies between 1.1 and 2.2  $\mu\text{m}$  over the foil width of 30 cm.

By taking a closer look at the comparison of the device performance with different material analyses, the following correlations for the 21-cm-wide analyzed area can be obtained: Due to the fact that Sample 2 has a slightly higher  $CGI$  in the middle (see Table I), the  $CGI$ -distribution over the foil, which is similar for both samples, leads to a Cu-rich region at the bottom of Sample 2. The cells of the bottom region are therefore shunted,

assumingly due to the formation of metallic copper selenides, as reported in [13]. Due to its overall lower  $CGI$ , Sample 1 has good homogeneity of the efficiency across the substrate width, although the thickness varies between 1.5 and 2.2  $\mu\text{m}$  and the  $CGI$  is in the range of 84%–94%. As reported by [14], this confirms a relatively large process window in terms of absorber thickness for the later fabrication of highly efficient CIGSe solar cells. The decrease of  $CGI$  from bottom to top seems to result in an increasing thickness of the copper-poor VC. We conclude this by the SEM-EDX measurement done with an acceleration voltage of 7 keV, which leads to an approximate analytical depth of 100 nm, shown in Fig. 8. The “top” and “mid” positions of Sample 1 and only the “top” position of Sample 2 reached a  $CGI_{\text{EDX-7kV}}$  between 54% and 57%. Whereas the “bot” position

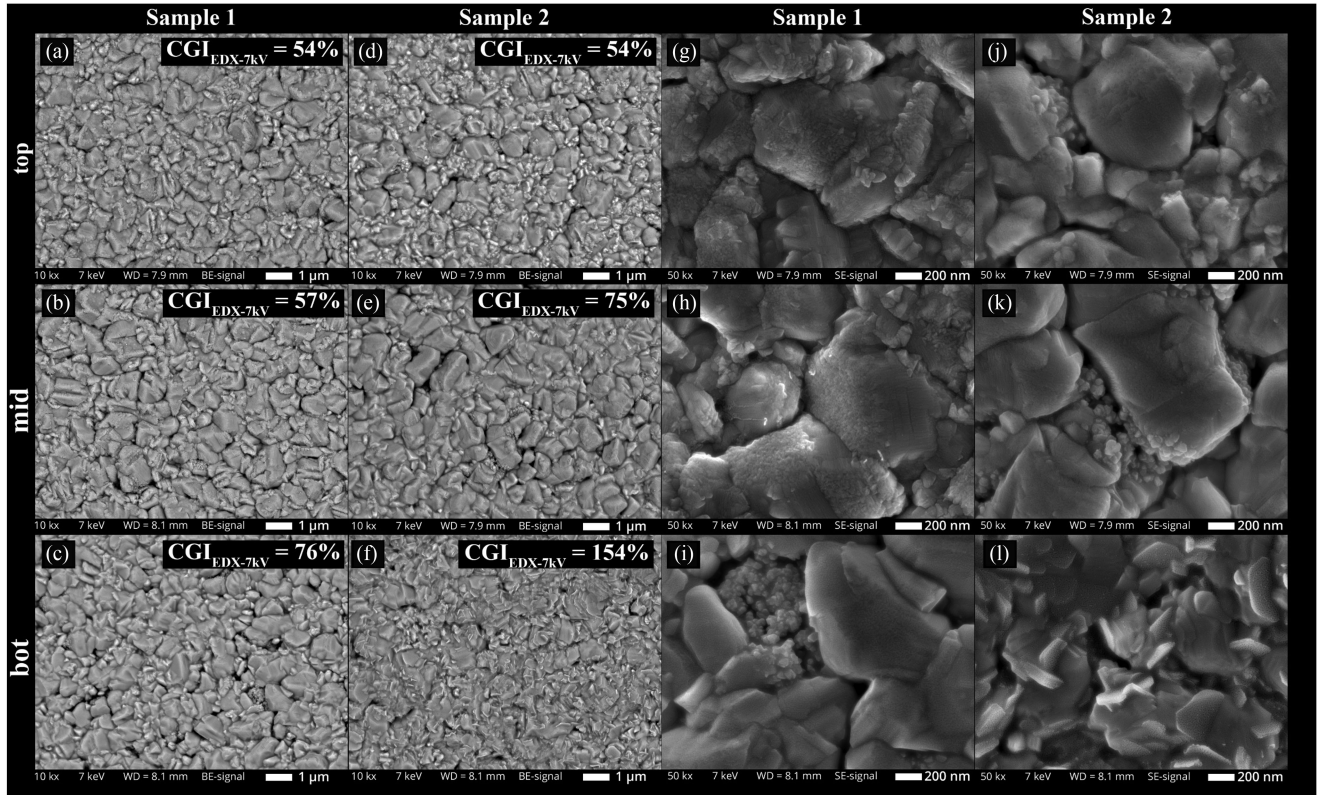


Fig. 8. (a)–(f) SEM backscatter electron images of the absorber surface of Samples 1 and 2 in the positions top, mid, and bot at 10k times magnification together with the  $CGI_{EDX-7kV}$  as measured by EDX using 7 kV acceleration voltage, which results in an analytical depth of about 100 nm. With respect to the assumed analytical depth, the  $CGI_{EDX-7kV}$  is in good agreement with the  $CGI$ -profiles measured by GD-OES (see Fig. 3). (g)–(l) SEM in-lens secondary electron images of the surface at 50k times magnification. We observe an extreme change of the morphology to sharp crystallites for (f) and (l) in comparison to (a)–(e) and (g)–(k), presumably due to CuSe segregation at the surface. (g), (h), and (j) Similar morphology while also having similar  $CGI_{EDX-7kV}$ . We also observe a similar morphology (regions of very small grains) for (i) and (k), while also showing a similar  $CGI_{EDX-7kV}$ .

of Sample 1 and the “mid” position of Sample 2 reached a  $CGI_{EDX-7kV}$  of about 75%. More details on the in-depth  $CGI$  are revealed by near-surface (approx. 500 nm deep)  $CGI$  profiles measured by GD-OES shown in Fig. 9. The thickest VC layer of over 200 nm is obtained for the “top” position of Sample 1. Similar thickness of about 100 nm is obtained for the “mid” position of Sample 1 and “top” position of Sample 2. Whereas the thinnest VC layer of approximately 50 nm is determined for the “bot” position of Sample 1 and the “mid” position of Sample 2. At the “bot” position of Sample 2, it exhibits a  $CGI$  above stoichiometry on the surface near region.

With SEM-EDX (Fig. 8) and GD-OES (Fig. 9), we identified a  $CGI$  of about 60% for the VC-layer. This results in a mixture of different Cu-deficient phases, such as  $Cu(In,Ga)_3Se_5$  and stoichiometric  $Cu(In,Ga)Se_2$ .

GI-XRD measurements indicate (Fig. 10) that at the “bot” position of Sample 2, a CuSe phase is detectable, which is identified by the ICDD pattern 00-034-0171. The main diffracted signal occurs from the pattern 99-00-0022 described in [15], which has an elemental formula of  $CuIn_{0.785}Ga_{0.22}Se_2$ . This result concurs well with the compositional results described. In addition, the depth-dependent change of the 112 peak position ( $2\theta = 26.835^\circ$ ) of the CIGSe phase was analyzed for both samples on each position (“top,” “mid,” and “bot”) by varying the incident angle

$\Omega$  from  $0.2^\circ$  to  $3^\circ$ . The peak was fitted with a pseudo Voigt function and the  $d$ -spacing was calculated by Bragg’s equation. As reported in [12] and [15]–[17], the  $d$ -spacing decreases with decreasing  $CGI$ . The decreasing of the  $d$ -spacing by increasing  $GGI$  is also known [15], [18]. With respect to these two effects, the change in the  $d$ -spacing in Fig. 11 coincides very well with the compositional depth profiling by GD-OES. Therefore, the lowest  $d$  can be identified for the two “top” measurement positions. While the “top” position of Sample 1 has a lower  $GGI$  but presumably a thicker VC, the “top” position of Sample 2 has a higher  $GGI$  with thinner VC, which results in a similar  $d$ -spacing behavior. The highest  $d$  at  $\Omega = 0.2^\circ$  results at the “bot” position of Sample 2, because of the CuSe and the absence of VC on the surface. For higher  $\Omega$ , the “top” position of Sample 1 indicates the highest  $d$  because of the lowest Ga concentration. The  $x$ -axis in Fig. 11 is log scaled due to the absorption law, as explained in detail in [16] and [19].

According to the literature, the surface morphology is prone to show a higher amount of smaller circular crystallites with decreasing  $CGI$  [17], [20]. This can be seen in Fig. 8, by comparing the SEM pictures (g), (h), and (j), showing a similar morphology while the corresponding regions also show similar  $CGI_{EDX-7kV}$ . We also observe a similar morphology (regions of very small grains) and  $CGI_{EDX-7kV}$  for (i) and (k). The SEM

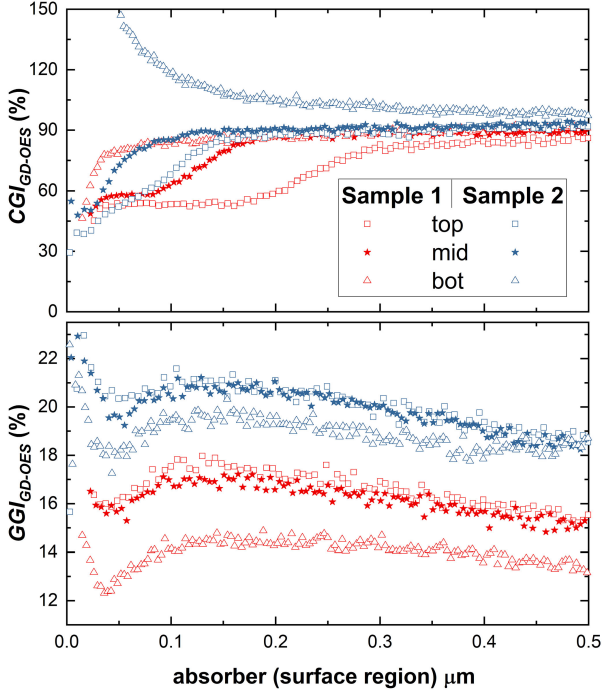


Fig. 9. CGI profiles of the surface near part (500 nm) measured by GD-OES of Samples 1 and 2 at three different positions. For the bottom region (bot) of Sample 2, a CGI higher than 100% is detected. This explains the shunted part of the analyzed area.

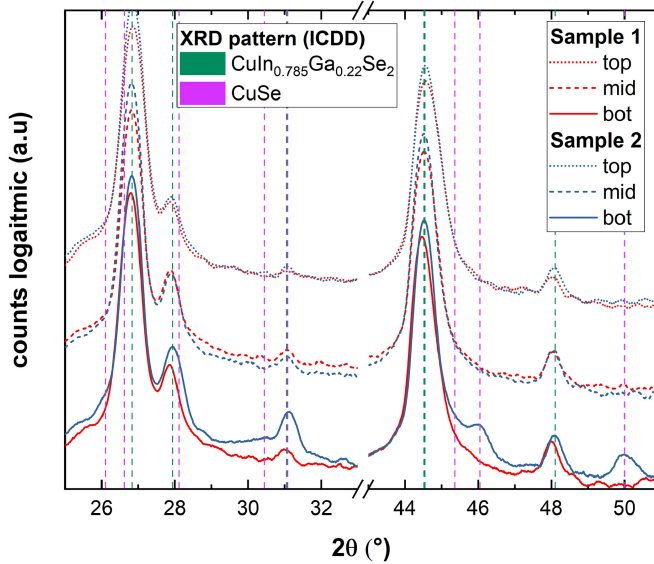


Fig. 10. GI-XRD diffractograms of Sample 1 and 2, each measured at the three previously defined positions. At the bottom measurement position of Sample 2, CuSe was identified. Dedicated peaks are marked by the dotted pink vertical lines.

images in Fig. 8(g)–(l) depict SEM in-lens secondary electron pictures of the surface at 50 000 times magnification. We observe an extreme change of the morphology to sharp crystallites for (f) and (l) in comparison to (a)–(e) and (g)–(k) due to the presence of CuSe at the surface.

From experiments, in which we separately determined the geometrical distribution of the metal and the selenium vapor,

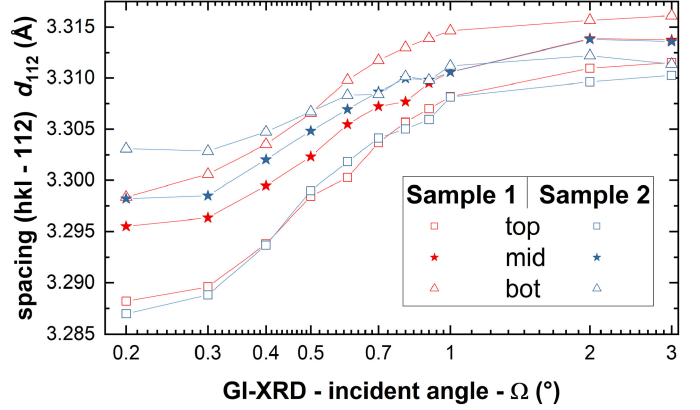


Fig. 11.  $d$ -spacing of the  $(hkl = 112)$  plane was evaluated for different incident angles  $\Omega$ . The 112 peak shifts to higher angles with increasing  $GGI$  and also with decreasing  $CGI$ . Therefore, the lowest  $d$  can be identified for the two “top” measurement positions. While the “top” position of Sample 1 has a lower  $GGI$  but a thicker VC, the “top” position of Sample 2 has a higher  $GGI$  with a thinner VC, both resulting in a similar  $d$ -spacing behavior. The highest  $d$  at  $\Omega = 0.2$  is found for Sample 2 at the “bot” position. In this area, Sample 2 shows no VC, but CuSe on the surface. For higher  $\Omega$ , the “top” position of Sample 1 shows the highest  $d$  because of its lower Ga content. This is consistent with the measured  $CGI$  and  $GGI$  by GD-OES. The lines between the points shall only help to identify the trend.

we found out that the metal vapor distribution proved to be symmetric, while an asymmetric selenium vapor distribution was determined. This leads to the assumption that the inhomogeneity of the  $CGI$  is caused by an asymmetric selenium vapor distribution. Possible explanations may be that the asymmetric selenium distribution can cause an asymmetric sputter yield at the magnetrons or influence re-evaporation effects during layer formation. Both effects would influence the resulting  $CGI$ . Especially concerning re-evaporation effects and layer growth, it has to be considered that the mean free path at a process pressure of  $\sim 3 \times 10^{-3}$  mbar is in the range of 1–10 cm and the distance between the graphite bar and the substrate varies between 33 and 45 cm. Therefore, the particles’ collisions cannot be neglected for the hybrid-CIGSe-process in comparison to a classical three-stage evaporating process.

#### IV. CONCLUSION

It has been shown that a double graded gallium profile in a CIGSe layer can be realized and reliably controlled when applying the hybrid-CIGSe-process by Sunplugged.

The power ratios for the In- and Ga-magnetrons in Steps 1 and 3 are shown to be the decisive value to be considered for optimizing the Ga profile, resulting in conversion efficiencies of upto 14.0% (w/o antireflective coating, active area value). We can confirm that the  $GGI$  is proportional to the photoactive bandgap and, therefore, also proportional to the resulting  $V_{OC}$  and inversely proportional to the  $j_{SC}$ . Further potential for improvement of the cell efficiency is given by the ongoing optimization of the Ga gradient. Moreover, alkali postdeposition treatments and improved buffer materials may increase the conversion efficiency as well.

Furthermore, we can conclude that the *GGI* shows good homogeneity, whereas the *CGI* shows a moderate homogeneity over the 30 cm width of the substrate foil applying the R2R hybrid-CIGSe-process. It has been observed that there may be a correlation between the *CGI* homogeneity and the asymmetry of the selenium vapor distribution; further investigations are ongoing to clarify that. We were able to confirm the influence of the Cu content on the crystal structure and on the surface morphology, described in previous publications [7], [11], [12], [15], [16], [21], and [22]. The influence of the Cu content on the conversion efficiency, at least in the range of the presented values, seems to be rather small for the analyzed range of about 85%–97%. This confirms the suitability of CIGSe absorbers for industrial usage, due to its wide process window. It is of high importance to guarantee a *CGI* below stoichiometry, due to the shunting behavior of copper selenides. Therefore, it seems to be convenient for industrial application to aim at a lower *CGI* in order to prevent formation of copper selenides at large-scale production.

#### ACKNOWLEDGMENT

The authors would like to thank M. Harnisch, S. Ghodbane, B. Gmeiner, and C. Kammerlander for the execution of the working steps at Sunplugged GmbH and J. Lauche, T. Münchenberg, T. Hänel, S. Stutzke, S. Ghaderi, Z. Salami, and D. Schewitz for assisting with the technical tasks at HZB.

#### REFERENCES

- [1] M. Nakamura *et al.*, “Cd-free Cu(In,Ga)(Se,S)<sub>2</sub> thin-film solar cell with record efficiency of 23.35%,” *IEEE J. Photovolt.*, vol. 9, no. 6, pp. 1863–1867, Nov. 2019.
- [2] M. Jošt *et al.*, “21.6%-Efficient monolithic perovskite/Cu(In,Ga)Se<sub>2</sub> tandem solar cells with thin conformal hole transport layers for integration on rough bottom cell surfaces,” *ACS Energy Lett.*, vol. 4, no. 2, pp. 583–590, 2019.
- [3] H. Shen *et al.*, “Mechanically-stacked perovskite/CIGS tandem solar cells with efficiency of 23.9% and reduced oxygen sensitivity,” *Energy Environ. Sci.*, vol. 11, no. 2, pp. 394–406, 2018.
- [4] M. Acciarri *et al.*, “Hybrid sputtering/evaporation deposition of Cu(In,Ga)Se<sub>2</sub> thin film solar cells,” *Energy Procedia*, vol. 10, pp. 138–143, 2011.
- [5] S. Binetti *et al.*, “Fabricating Cu(In,Ga)Se<sub>2</sub> solar cells on flexible substrates by a new roll-to-roll deposition system suitable for industrial applications,” *Semicond. Sci. Technol.*, vol. 30, no. 10, 2015, Art. no. 105006.
- [6] M. Acciarri *et al.*, “CIGS thin films grown by hybrid sputtering-evaporation method: Properties and PV performance,” *Sol. Energy*, vol. 175, pp. 16–24, 2018.
- [7] N. Weinberger *et al.*, “New approach for an industrial low-temperature roll-to-roll CI(G)Se hybrid sputter coevaporation deposition process,” *J. Vac. Sci. Technol. A*, vol. 38, no. 3, 2020, Art. no. 33201.
- [8] N. Weinberger *et al.*, “Realizing double graded CIGSe absorbers with the R2R Hybrid-CIGSe-process,” in *Proc. 47th IEEE Photovolt. Specialists Conf.*, 2020, pp. 1–4.
- [9] K. Endres, M. Mennig, M. Amlung, A. Gier, and H. Schmidt, “Enhancement of fracture strength of cutted plate glass by the application of SiO<sub>2</sub> sol-gel coatings,” *Thin Solid Films*, vol. 351, no. 1–2, pp. 132–136, 1999.
- [10] T. Kodalle *et al.*, “Glow discharge optical emission spectrometry for quantitative depth profiling of CIGS thin-films,” *J. Anal. At. Spectrom.*, vol. 34, no. 6, pp. 1233–1241, 2019.
- [11] R. Caballero *et al.*, “Cu deficiency in multi-stage co-evaporated Cu(In,Ga)Se<sub>2</sub> for solar cells applications: Microstructure and Ga in-depth alloying,” *Acta Materialia*, vol. 58, no. 9, pp. 3468–3476, 2010.
- [12] R. Caballero *et al.*, “Investigation of Cu(In,Ga)Se<sub>2</sub> thin-film formation during the multi-stage co-evaporation process,” *Prog. Photovolt: Res. Appl.*, vol. 21, no. 1, pp. 30–46, 2013.
- [13] T.-P. Hsieh *et al.*, “Effects of residual copper selenide on CuInGaSe<sub>2</sub> solar cells,” *Solid-State Electron.*, vol. 56, no. 1, pp. 175–178, 2011.
- [14] W. Li *et al.*, “Improvement of the crystallinity and efficiency of wide-gap CIGS thin film solar cells with reduced thickness,” *Materials Lett.*, vol. 244, pp. 43–46, 2019.
- [15] M. Souilah, A. Lafond, C. Guillot-Deudon, S. Harel, and M. Evain, “Structural investigation of the Cu<sub>2</sub>Se–In<sub>2</sub>Se<sub>3</sub>–Ga<sub>2</sub>Se<sub>3</sub> phase diagram, X-ray photoemission and optical properties of the Cu<sub>1–z</sub>(In<sub>0.5</sub>Ga<sub>0.5</sub>)<sub>1+z/3</sub>Se<sub>2</sub> compounds,” *J. Solid State Chem.*, vol. 183, no. 10, pp. 2274–2280, 2010.
- [16] I. M. Kötschau and H. W. Schock, “Depth profile of the lattice constant of the Cu-poor surface layer in (Cu<sub>2</sub>Se)<sub>1–x</sub>(In<sub>2</sub>Se<sub>3</sub>)<sub>x</sub> evidenced by grazing incidence X-ray diffraction,” *J. Phys. Chem. Solids*, vol. 64, no. 9–10, pp. 1559–1563, 2003.
- [17] B. Namnuan, V. Amornkitbamrung, and S. Chatraphorn, “Effects of Cu(In,Ga)<sub>3</sub>Se<sub>5</sub> defect phase layer in Cu(In,Ga)Se<sub>2</sub> thin film solar cells,” *J. Alloys Compounds*, vol. 800, pp. 305–313, 2019.
- [18] S. Lehmann *et al.*, “Long-range structure of Cu(In<sub>x</sub>Ga<sub>1–x</sub>)<sub>3</sub>Se<sub>5</sub>: A complementary neutron and anomalous x-ray diffraction study,” *J. Appl. Phys.*, vol. 109, no. 1, 2011, Art. no. 13518.
- [19] I. M. Kötschau and H. W. Schock, “Compositional depth profiling of polycrystalline thin films by grazing-incidence X-ray diffraction,” *J. Appl. Crystallogr.*, vol. 39, no. 5, pp. 683–696, 2006.
- [20] T. Nishimura, S. Toki, H. Sugiura, K. Nakada, and A. Yamada, “Interfacial quality improvement of Cu(In,Ga)Se<sub>2</sub> thin film solar cells by Cu-depletion layer formation,” *Appl. Phys. Express*, vol. 9, no. 9, 2016, Art. no. 92301.
- [21] E. Haubold *et al.*, “Short-range versus long-range structure in Cu(In,Ga)Se<sub>2</sub>, Cu(In,Ga)<sub>3</sub>Se<sub>5</sub>, and Cu(In,Ga)<sub>5</sub>Se<sub>8</sub>,” *J. Alloys Compounds*, vol. 774, pp. 803–812, 2019.
- [22] H. Rodriguez-Alvarez *et al.*, “Formation of CuInSe<sub>2</sub> and CuGaSe<sub>2</sub> thin-films deposited by three-stage thermal co-evaporation: A real-time X-Ray diffraction and fluorescence study,” *Adv. Energy Mater.*, vol. 3, no. 10, pp. 1381–1387, 2013.